Supplementary Information

Dynamics of colloid accumulation under flow over porous obstacles

Matthieu Robert de Saint Vincent, Manouk Abkarian, and Hervé Tabuteau

S1 Péclet number at the pore entrance

We computed the velocity distribution in the vicinity of modelled pores with Comsol Multi-physics. Pores were drawn in the plane respecting the experimental geometry, and the Stokes equation was solved in an automatically-generated 2D mesh, imposing an inflow velocity $v_0 = Q/S$ (with S the cross section of the real channel and Q in the experimental range; Reynolds number Re $\sim 10^{-2}$–1 therein) along the $-y$ direction. Typical velocity maps are shown on Fig. S1 for the two types of pores considered. The calculated data were then exported to a Matlab-written routine to estimate the velocity $v(x, y)$ at specific locations. We may then deduce the local Péclet number, Pe $= 6\pi\eta a^2 v/(k_{\mathrm{B}} T)$, where $\eta = 1$ mPa s is the viscosity of water, $a = 2$ μm the particle radius and $T = 295$ K the room temperature.

We first estimated, for reference, the Péclet number experienced by a particle incident to an empty pore, 2 μm upstream of the apex on the centreline as represented by the crosses in the velocity maps on Fig. S1. The evolution of the calculated Péclet numbers with the imposed Q (more specifically, v_0) is represented on Fig. S1, both for single (green dots) and sheltered pores (blue squares). In single pores, Pe increases faster than linearly with the imposed velocity. Single pores actually feature a handlebar-shaped transition zone near the pore entrance, where the velocity rapidly decreases. This shape progressively flattens as v_0 increases (see Section S2 below), increasing by the way the apparent velocity at the reference point.

The evolution of Pe with v_0 in sheltered pores (here, $D = 100$ μm, but rather similar values were found between 50 and 200 μm) is more surprising. The initial increase slows down till 40 mm s^{-1}, then Pe slightly decreases, before a very fast increase (close to v_0^3) finally takes place above 80 mm s^{-1}. This evolution is likely due to the greater complexity of the flow pattern in the wake of the obstacle compared to the single pore case.

The choice of an empty pore as reference for Péclet numbers is somewhat remote from the experimental situation, which consists of already obstructed pores. This choice, however, is made necessary since we do not know the permeability of the clog. Nevertheless, we estimated the effect of reducing the permeability of the pore by inserting a network of circular obstacles therein. Figure S2 compares velocity maps in open (left half) and partly obstructed pores (right half). Although both flow patterns have a qualitatively similar shape, the transition zone is shifted downstream of the obstructed pore. This effect, which locally accelerates the flow near the pore entrance, competes with a global slowing down along the centreline due to the presence of obstacles. As a result, the local velocity (and thereby Pe) calculated at the reference point are smaller than in the open pore case, to an extent that depends on the clog permeability, up to a factor of 20 for a closed (non-porous, flat-topped) pore. Besides, the Pe(v_0) supralinear trend is preserved regardless of the permeability.

S2 Velocity profiles

Understanding the hydrodynamic forces experienced by incident particles requires to estimate the local velocity gradients on a so-called interception line, transverse to the flow and located
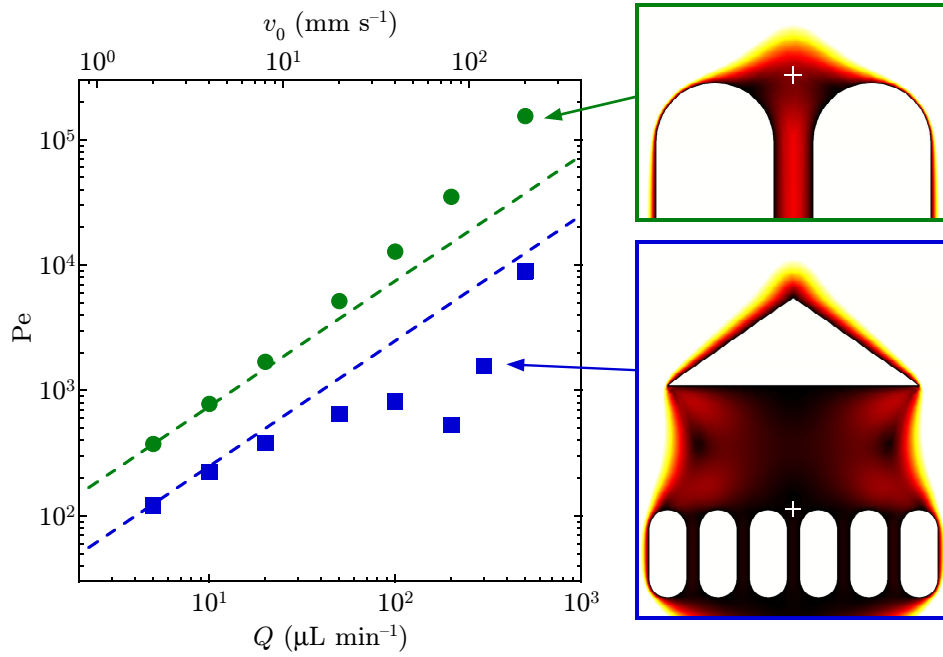
Figure S1: Evolution of the Péclet number calculated at the pore entrance (white crosses in the velocity maps) with the imposed flow rate Q (or equivalently, inflow velocity v_0), for a single pore (dots, upper map) and a sheltered pore (squares, lower map). The dashed lines are linear fits to the low-Q limit drawn as guides to the eye.
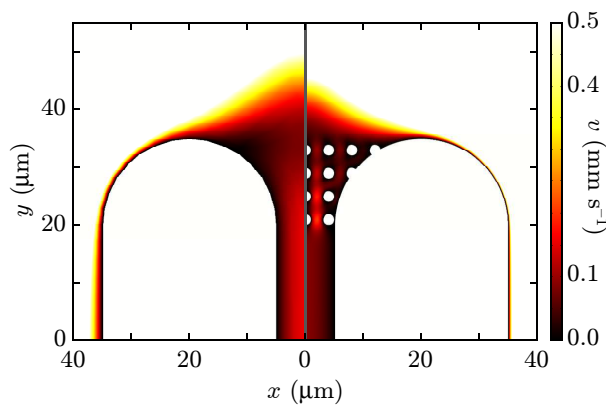

Figure S2: Influence of the obstacle porosity on the flow pattern: unclogged pore (left), porous clog (right). The obstacles inserted into the pore have a diameter of 1 μm. Inflow velocity $v_0 = 8$ mm s^{-1}; the colour scale is clipped to emphasise local variations.
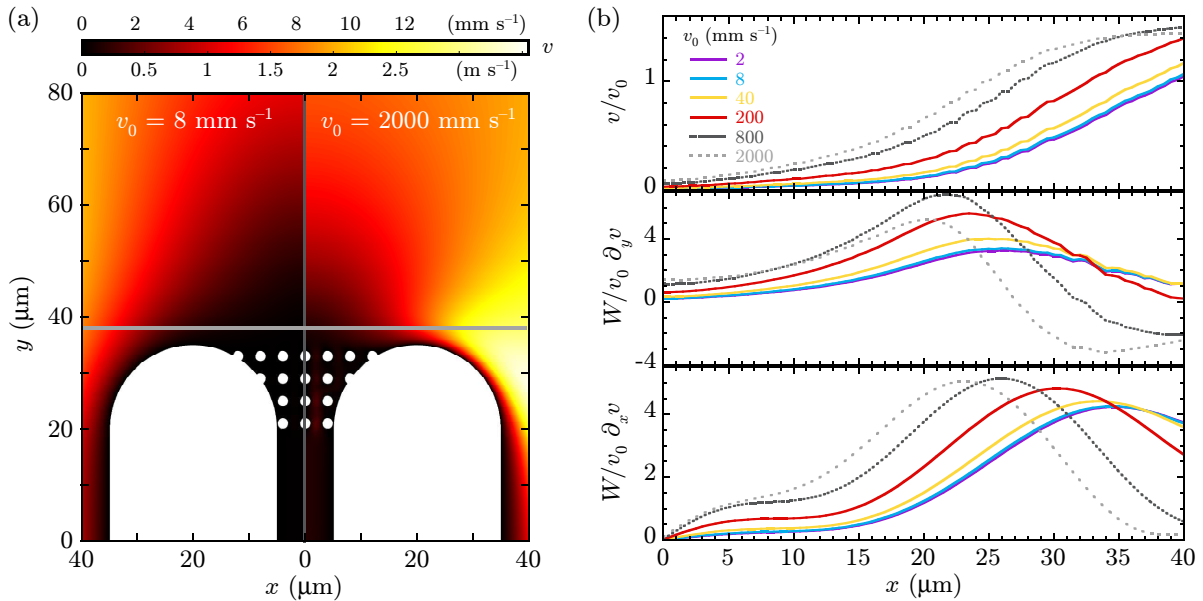
Figure S3: (a) Representative velocity maps for $v_0 = 8$ (left) and 2000 mm s^{-1} (right). (b) Evolution of the reduced velocity (top), axial (middle) and transverse (bottom) velocity gradients profiles over the interception line [horizontal line on Fig. S3 (a)] with the inflow velocity v_0.

nearby the apex (we chose 1.5 particle radius upstream, horizontal grey line on Fig. S3). A wide range of incident velocities, covering the whole experimental range and beyond, was considered to characterise how the flow pattern evolves with v_0 in experiments. The velocity profile along the interception line [in light grey on Fig. S3 (a)] was obtained by slicing the x axis in small steps (typically, 0.5-µm wide) and selecting the closest mesh element in each. We then calculated the velocity gradient components along the x and y directions. The transverse gradient, $\partial v/\partial x$, was simply obtained by derivating the $v(x)$ profile fitted by a high-order (typically, 10) polynomial function. The procedure for calculating the axial velocity gradient, $\partial v/\partial y$, is slightly less straightforward. In each $x = $ cst. slice, the axial velocity profile was retrieved as described above, then again fitted over a $\sim$ 5–10 µm-long stripe by a polynomial function — care was taken to avoid the pore. The value of the derivative at the closest y to the interception line was then kept for each axial slice. Velocity and velocity gradient components were then normalised by v_0 and v_0/W to make comparisons easier.

Figure S3 (a) represents the velocity maps calculated for a moderate and a very high velocities, $v_0 = 8$ mm s^{-1} (left half), and $v_0 = 2$ m s^{-1} (right half). The shape of the flow pattern strongly changes: in the fastest case, the axial variation strengthens along the centreline, and a high velocity region sharply emerges near the outer part of the pore. The velocity profile along the interception line represented on Fig. S3 (b) (top row) shows this evolution as the maximal velocity gradually shifts inwards as v_0 increases. The maxima of the axial and transverse velocity gradients [Fig. S3 (b), middle and bottom row respectively] are both gradually shifted inwards as well. In addition, at very high velocities (beyond 200 mm s^{-1}) the axial gradient reverses at the outer part of the pore, signature of the sharp high velocity inclusion mentioned above. This reversal means that particles entering this region should experience a backwards pushing force, preventing any particle deposition in the outer part of the pore. Though, we did not explore this high-velocity regime experimentally.

Finally, the inwards shifting of the gradient maxima does not dramatically affect the ratio of their components (not represented here), besides the appearance of the negative axial component at high velocities. We shall also mention, at the very highest velocity investigated (2 m s^{-1}), the suppression of the local minimum near $x \simeq 13$ µm (see Fig. 5), which suggests that particle

capture in this regime would only occur within the gap.

S3 Supplementary movies

M1. Building up of an aggregate, corner shape. $I = 0$ mM, $Q = 10$ μL min^{-1}, $\phi = 10^{-3}$ [Fig. 2 (b), image i]. Total duration of the movie in real time: 1404 s.

M2. Building up of an aggregate, flat shape. $I = 50$ mM, $Q = 20$ μL min^{-1}, $\phi = 10^{-3}$ [Fig. 2 (c), image iii]. Total duration of the movie in real time: 8067 s.

M3. Building up of an aggregate, finger shape. $I = 50$ mM, $Q = 200$ μL min^{-1}, $\phi = 2 \times 10^{-4}$ [Fig. 2 (c), image iv]. Total duration of the movie in real time: 2664 s (the flow is turned off after 2430 s, showing the dilation of the structure upon PDMS relaxation).

M4. Building up of an aggregate, tip shape. $I = 50$ mM, $Q = 500$ μL min^{-1}, $\phi = 2 \times 10^{-4}$ [Fig. 2 (c), image v]. Total duration of the movie in real time: 903 s (the flow is turned off after 757 s, then the height of the PDMS channel decreases, which leads to the vertical compression of the structure followed by a lateral expansion).

M5. Withdrawal of a sheltered aggregate. $I = 0$ mM, $D = 100$ μm. Total duration of the movie in real time: 80 s.

M6. Withdrawal of a sheltered aggregate. $I = 0$ mM, $D = 150$ μm. Total duration of the movie in real time: 30 s.

M7. Sheltered aggregate, evolution after the flow was turned off. $I = 0$ mM, $D = 50$ μm. Total duration of the movie in real time: 110 s. Note the particles in the outer part of the aggregate jiggling under thermal agitation, and some rearrangements occurring within the structure.